IoT Challenges: Antenna Efficiency and TIS Measurements in a Reverberation Chamber

Hubrechsen, A.

Award date:
2019

IoT Challenges: Antenna Efficiency and TIS Measurements in a Reverberation Chamber

Anouk Hubrechsen

***Abstract*—Recently developed Internet-of-Things (IoT) applications can cause new challenges in reverberation-chamber measurements, due to the introduction of a narrowband communication protocol, Narrowband Internet-of-Things (NB-IoT), and the introduction of new antenna designs. The first can result in higher uncertainties in the chamber transfer function and Total Isotropic Sensitivity (TIS), which we will show with preliminary results. The latter can contain designs with high losses or high frequency selectivity. Such characteristics imply low efficiencies at some frequencies which makes it more challenging to accurately measure them, since noise can start to affect the measured S-parameters, hence the antenna efficiency estimate when the one-, two-, or three-antenna method is used. We provide an extensive explanation of this issue, and we provide a solution. We provide novel methods for determining uncertainty for antenna efficiency and TIS. This work will inform users on previously unknown challenges and will provide means of resolving them.**

***Index Terms*—Antenna Efficiency, Chamber Transfer Function, Internet of Things, Noise, Reverberation chambers, Total Isotropic Sensitivity, Uncertainty**

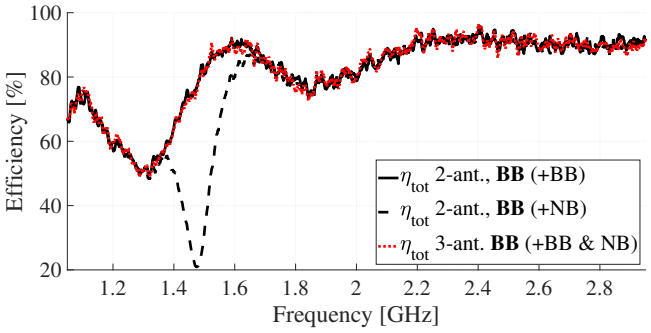

Fig. 1. Total efficiency of a broadband (BB) antenna, measured with a narrowband (NB) and/or BB antenna as a measurement antenna, for both the two- and three-antenna method. The two-antenna method efficiency estimate calculated with a NB antenna shows large differences with the three-antenna method estimate.

I. Introduction

5G-and-beyond requirements are pushing for new innovations in order to meet current society demands such as lower latency, increased capacity and higher data rates. A significant part of meeting these demands in 5G-communications will be through Internet-of-Things (IoT) or machine-to-machine (M2M) applications, which are well on their way of surpassing the current amount of mobile communication devices, and will largely operate in the lower-5G bands (600 MHz - 6 GHz) [1] [2]. There are two characteristics that are typical for IoT applications we will focus on. The first one being Total Isotropic Sensitivity (TIS) and the second one antenna efficiency.

TIS is a measure of the sensitivity of a device, or the minimum power a device can receive while still maintaining a connection with certain bit-error rate (BER). Using a reverberation chamber (RC) for characterizing TIS has gained popularity in recent years due to its flexible test volume and rapid, low-cost measurements. These characteristics are much desired for measuring IoT devices, and since these are generally mass-produced and low-cost, they require measurement techniques that meet those aspects. These devices will use the Narrowband Internet-Of-Things (NB-IoT) protocol [3] - [7]. For IoT, it is preferable to use such narrowband devices, since these devices use very low data rates and they need to coexist with many other of these devices. However, the narrowband nature of this protocol can cause numerous challenges for measurements in a reverberation chamber due to its rapidly changing frequency response.

To obtain a TIS estimate obtained from an RC measurement one does not need to know the antenna efficiency of the device under test (DUT), as the antenna is stated as part of the device [8]. However, when one is aiming to develop a new standard, or when one is designing an antenna for such a device, it is critical to know its antenna efficiency. This metric is more crucial than other metrics, such as directivity, since IoT devices are expected to be mainly used in highly reflective, scattering environments [9]. New IoT applications can introduce less-conventional antenna designs, such as narrowband antennas that are tunable over frequency, and those operating in multiple bands but with a high rejection band [9]. These characteristics are preferable for IoT, since separate filters are no longer needed per band, because these are integrated in the antenna characteristics. This saves space and allows for more flexibility in frequency allocation. However, characterizing such devices can cause new challenges, since they can have high losses or can be highly mismatched for certain bands within their total frequency range of operation. Antenna efficiency can be characterized both in an anechoic chamber (AC) and an RC [10] - [17]. Multiple techniques have been proposed to determine efficiency in an RC, both with and without a dependence on a reference antenna with a known efficiency.

Popular methods that do not depend on the use of a reference antenna with a known efficiency are the one-, two-, and three-antenna methods first presented in [14]. They are based on the difference in the RC's quality factor (Q) between the frequency and time domain, where the latter does not include the early-time behavior of the RC [18] [19], while the former does. The difference between the two can be directly related to antenna efficiency. Especially the two-

antenna method is a preferable technique for determining antenna characteristics in IoT applications, since it relies on less assumptions than the one-antenna method, but it takes significantly less measurement time compared to the three-antenna method, leading to a fast, hence low-cost measurement. It has been shown that these methods can provide accurate results for low-loss and broadband antennas [20] [21]. However, as we will show, large discrepancies in efficiency can occur when these methods are used with highly-mismatched or high-loss antennas. An example is presented in Fig. 1. This figure shows a large difference between the total efficiency for a broadband horn estimated with the two-antenna method when the second antenna is narrowband, as compared to a case where the second antenna is a broadband antenna or compared to a case with the three-antenna method. In this case, the discrepancy occurs near the rejection band of the narrowband antenna.

Before the popularity of narrowband antennas, this issue was mostly left unnoticed since these methods were mainly used for the characterization of broadband and low-loss antennas. However, with an increase in IoT applications, we are finding the need to characterize less-conventional antenna designs, which, as shown in Fig. 1, can cause unexpected issues. To the author's knowledge, only one earlier work has reported problems with the one- and two-antenna method, but the origin of this issue was not documented in that work [16].

This paper consists of two parts. In the first part (Section II - VI), we will show that issues occur with the one-, two-, and three-antenna method when the signal-to-noise ratio (SNR) of the S-parameters drops too far, and in the second part (Section VII - IX) we will show new IoT challenges in measuring TIS. We introduce a new way of describing stirred energy with contributions from noise in Section II, where we describe the theory and assumptions behind the one-, two- and three-antenna methods. In Section III, we provide an approach for determining uncertainties for the three-antenna method by updating such an existing approach for the two-antenna method. We also provide a novel time-saving method for applying systematic uncertainties on multiple independent realizations. In Section IV, we provide efficiency results for multiple use cases, we show a new approach to overcome the constraint of having a short time interval for chamber-decay time and we provide scatter plots that show that noise affects the stirred energy. The latter is verified in Section V, where we present a novel noise model. In Section VI, we summarize how to recognize the issue and how to solve it. Part II starts in Section VII, where we focus on the theory behind TIS. In Section VIII, we show a novel proposed method of determining uncertainty for TIS and in Section IX, we show preliminary uncertainty results and the work is concluded in Section X.

PART I: Noise Effect in Antenna Efficiency Measurements

Antenna efficiency is an important metric in IoT applications, since it is needed for development and verification of new antenna designs and new measurement methodology, such as measuring TIS for NB-IoT. We will explain the effect of noise on antenna efficiency for such IoT applications.

II. Theory

In this section, we first review the theory and assumptions behind the one-, two- and three-antenna methods, and the constraints they bring with them. After, a new way of describing stirred energy that includes noise is introduced.

A. Three-Antenna Method

When one uses three antennas, the equations of the three-antenna method used to estimate total efficiency are given by

$$\eta_i^{\text{total}} = \sqrt{\frac{C_{RC}}{\omega\tau_{RC}}}\sqrt{\frac{\langle|S_{ij,s}|^2\rangle\langle|S_{ik,s}|^2\rangle}{\langle|S_{jk,s}|^2\rangle}}, \tag{1}$$

where $\langle|S_{ij,s}|^2\rangle$, $\langle|S_{ik,s}|^2\rangle$ and $\langle|S_{jk,s}|^2\rangle$ are the variances of the transmission coefficients between two antennas connected to VNA ports i and j, i and k, and j and k, respectively, and where $i \neq j \neq k$. $C_{RC} = \frac{16\pi^2 V}{\lambda^3}$, where V is the chamber volume in m^3, λ is the wavelength in m, and τ_{RC} is the chamber decay time in s. These equations can be directly related back to the fundamental theory discussed in [22] and [23]. They only rely on the assumption that *the losses in the RC are dominated by the chamber walls*. This causes constraints in two ways:

1) This technique is derived from equations that assume an unloaded (or very lightly loaded) chamber. Since chamber wall losses are no longer dominant with loading [24], this technique is not supposed to be applied to loaded chambers.
2) It can become problematic to determine τ_{RC} when antenna losses become dominant, due to the short time interval where the excited power drops down to the noise floor [14] [16] [26]. Theoretically, the length of the time interval should not matter, however, using a short calculation time interval can cause increased uncertainties since fewer data samples are used. In Section III we will show an approach of determining the chamber decay time in such a way that this constraint does not cause problems anymore.

It should be noted that there may be other constraints as well, but these are known to be the key issues with these methods.

B. Two- and One-Antenna Method

By applying an additional assumption about enhanced backscattering, which assumes that the enhanced backscattering does not change over position, orientation and polarization in the chamber, the two-antenna method can be derived from the three-antenna method where the enhanced backscattering constant (e_b) may be given by

$$e_b = \frac{\sqrt{\langle|S_{ii,s}|^2\rangle\langle|S_{jj,s}|^2\rangle}}{\langle|S_{ij,s}|^2\rangle}, \tag{2}$$

where $\langle|S_{ii,s}|^2\rangle$ and $\langle|S_{jj,s}|^2\rangle$ are the variances of the reflection coefficient of an antenna attached to port i and j of the

VNA, respectively, and where $i \neq j$. When (2) is substituted in (1), we obtain the equations for the two-antenna method, given by

$$\eta_i^{\text{total}} = \sqrt{\frac{C_{RC}}{\omega\ e_b} \frac{\langle |S_{ii,s}|^2 \rangle}{\tau_{RC}}}. \tag{3}$$

For an ideal, well-stirred chamber, $e_b = 2$ everywhere in the chamber [27]. The one-antenna method in [14] is based on this assumption. However, earlier work has shown that these values usually deviate from $e_b = 2$, and it has been shown that e_b can vary over position [28]. The two-antenna method does not assume the chamber to be ideal, but it does assume e_b to be the same over position. Therefore, the two-antenna method can be less accurate than the three-antenna method [28]. Nonetheless, this assumption does not introduce any constraints on the antenna performance, so the method should work for all antenna types. However, as shown in Fig. 1, this is not the case for this method, so this method has an additional, previously unestablished, constraint related to noise which we will discuss in Section IV, V and VI.

C. Stirred Energy Component

All S-parameter measurements that are performed in an RC consist of a stirred and unstirred energy component. Unstirred energy is defined as the contribution to the received power from waves that have not interacted with a mode stirrer. This could be due to "direct-path energy" contributions, but also due to "reflected-energy contributions". Stirred energy is defined as the contribution to the received power from waves that has interacted with a paddle or has changed due to position or polarization stirring, hence it is different for every mode-stirring sample. Unstirred energy introduces a high correlation component, which must be accounted for in RC measurements involving loaded chambers [24]. However, it is common practice to reduce the unstirred energy contributions from antenna measurements, for example by position stirring. As shown in [29], the stirred-energy component can be obtained by

$$S_{ij,s} = S_{ij} - \langle S_{ij} \rangle, \tag{4}$$

where $\langle S_{ij} \rangle$ is the unstirred energy component of S_{ij} and i and j the ports where the antennas are connected to the VNA and where i can be equal to j. This procedure is illustrated in Fig. 2 for a measurement of S_{21}. It should be noted that the unstirred energy component is much higher when $i = j$, since a large part of the unstirred energy component consists of the reflection coefficient of the antenna, whereas only unstirred energy from chamber effects contributes to the unstirred energy component for $i \neq j$. In literature, the points in the scatter plot in Fig. 2 are considered as contributions from the different paddle positions acting as a random variable even though the paddle contributions are not truly random, since the variation in the RC channel is deterministic and repeatable from one measurement to the next. However, noise from the RC, antennas or instrumentation acts as a random variable as well and hence, contributes to the variance of the scatter plot. Therefore, the variance can be written as a combination of contributions from the paddles and the noise as

$$\langle |S_{ij,s}|^2 \rangle = \langle |S_{ij,\text{paddles}} + S_{ij,\text{noise}} - \langle S_{ij} \rangle|^2 \rangle, \tag{5}$$

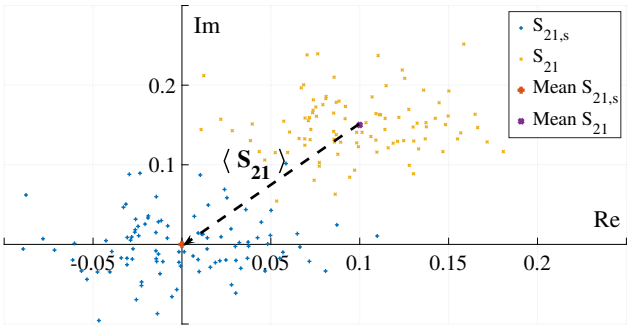

Fig. 2. Illustration of the procedure used to obtain $S_{21,s}$ from S_{21}, as used in the one-, two-, and three-antenna method.

where $S_{ij,\text{noise}}$ and $S_{ij,\text{paddles}}$ are the contributions to the stirred energy by the noise and the paddles, respectively. For low-loss antennas, $S_{ij,\text{noise}} \ll S_{ij,\text{paddles}}$, so the contribution of the noise on the variance becomes negligible. However, for high-loss antennas, this may not be the case. When antenna efficiency is very low, the paddle contribution to the variance can be similar or even lower than the contribution of the noise. This is because the noise variance is non zero if we assume gaussian noise. The noise mean is expected to be approximately zero for enough mode-stirring samples, so $\langle S_{ij} \rangle$ is not expected to be affected by the noise. Since research on noise in an RC has yet to be performed, it is unknown what its effect on the variance is. However, we expect that the contribution can vary for different paddle positions, but also for different turntable position due to movement of cables. Therefore, we need to look at the effect on uncertainty. Next, we show a novel method for determining such uncertainties.

III. Measurement Uncertainty

In this section, we present an updated approach for estimating uncertainty for antenna efficiency using the NIST Microwave Uncertainty Framework (MUF) [30]. We extend the approach for estimating uncertainty for the two-antenna method presented in [25] to work for the three-antenna method, and we introduce a novel approach of combining uncertainties due to random and systematic effects. First, we briefly review the approach for determining VNA calibration uncertainty for the two-antenna method in Part A. This is a systematic effect. We then demonstrate a method to extend it to the three-antenna method. Second, we show the approach for determining the uncertainty due to lack of spatial uniformity in Part B, which is determined from the differences between multiple independent realizations [31]. This is a random effect. Last, we combine the two in Part C. The process is shown in Fig. 3. It should be noted that the names 'Part A, B, and C' are unrelated to the terminology for Type A and B uncertainties.

- PART A: We obtain the calibration uncertainty in a similar way as described in [25] by using the MUF. However, since we developed this method with a three-sampler VNA, the switch terms are unknown and we cannot determine uncertainties from a three-port measurement. Therefore, we perform a three-channel measurement, where

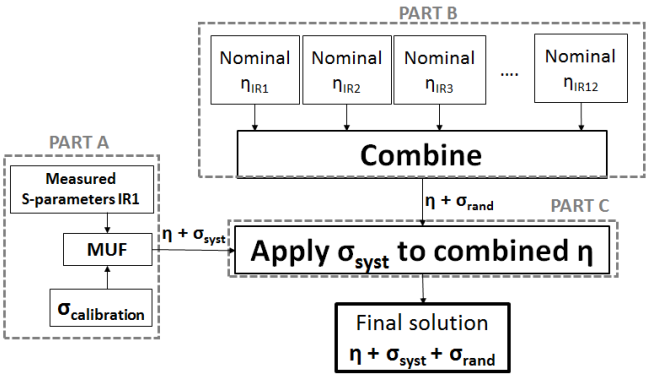

Fig. 3. A novel procedure for determining antenna efficiency uncertainty. We use the uncertainties due to a systematic effect of one independent realization (IR) and apply it to a combined nominal value with uncertainties due to a random effect acquired from all 12 IRs.

each channel contains a two-port measurement between two of the three ports. The method consists of three steps. First, we obtain the raw calibration uncertainty from the electronic calibration module by measuring, after calibration, mechanical SOLT standards. We also take the mechanical standards uncertainties into account which are defined by a model of these standards [32]. Since we only measure this once, we only take the uncertainties due to a *systematic* effect of the electronic calibration module into account. Second, we apply the calibration uncertainty to the measured S-parameters. This process is repeated for all three two-port measurements. Last, we combine all ports into one three-port measurement and we calculate efficiency using the S-parameters including uncertainties to obtain the uncertainties of the VNA calibration on efficiency. The MUF provides uncertainty estimates determined by using both a Monte Carlo (MC) analysis and a sensitivity analysis. Due to the non-linearity in the operators used in (1) and (3), we have used the MC approach. We used 100 MC simulations for each step, which has been proven to be sufficient for this case [25].

- PART B: To obtain this component of uncertainty, we calculate the efficiencies separately for 12 independent realizations, which will be more extensively explained in the next section. These are uncertainties due to a *random* effect. A coverage factor is applied to compensate for uncertainties due to the limited amount of independent realizations [33]. This part of the process is shown as part B in Fig. 3. We expect this component of uncertainty to be mostly affected by a lack of spatial uniformity. Therefore, we refer to this component of uncertainty as such. However, as we will show, this can contain other effects as well.
- PART C: As a last step in estimating uncertainty, we introduce a new way of combining the calibration and independent realization uncertainties. Since we only determine the uncertainties from the electronic calibration module once, and use the same uncertainties for the mechanical standards as well, we expect similar uncertainties for all independent realizations. Therefore, in part C of the process, we can use the uncertainties due to the systematic effect that were calculated for one independent realization in part A, and we can apply it to the combined efficiency with uncertainties due to a random effect that were calculated in part B. This ends up in one efficiency estimate that includes uncertainties due to both effects. This method saves time, since calibration uncertainties only have to be calculated once, instead for every independent realization.

In all efficiency results shown, we use the the 2σ deviation from the mean, or 95 % confidence interval [33], as a measure of the combined uncertainty. Next, we show the measurement setup used to calculate efficiency, and the efficiency results for different use-cases including uncertainties obtained using this method.

IV. Experimental and Modeled Results

This section illustrates the effects of a low SNR on an estimate of antenna efficiency, by providing measurements of different IoT use-cases, scatter plots, and models.

A. Measurements using the 2- and 3-antenna method

All measurements were performed in an RC located at the National Institute of Standards and Technology (NIST), with dimensions 4.74 x 4.13 x 5.18 m^3 and is shown in Fig. 4. The RC has one horizontal paddle and one vertical paddle for paddle stirring, and a turntable for position stirring. To lower the uncertainty, it is desirable to have as many mode-stirring samples as possible, while still ensuring low correlation between the samples [24]. Typically, a minimum of $P = 9$ turntable positions is required [24]. Therefore, both stirrers were varied over 10 different stepped positions, and the turntable over 12, resulting in 12 low-correlated independent realizations with 100 low-correlation mode-stirring samples each. From these independent realizations, we obtained uncertainties due to a lack of spatial uniformity. We calculated a best estimate for efficiency by taking the average of all independent realizations.

A VNA was used with an IF BW of 1 kHz, 100 kHz frequency spacing and 10 μs dwell time. The calibration reference plane was brought up to the connectors of the antennas by using an N-type electronic calibration module. The

Fig. 4. Setup in the NIST RC. Due to the height of the chamber, the horizontal paddle is not visible in this picture, but it is situated on the top left.

uncertainties caused by this type of calibration are discussed in Section IV. All measurements were performed in the 1 GHz - 3 GHz frequency range, since the frequency-reconfigurable antenna in one of the use-cases is reconfigurable within this frequency range. We discuss three use-cases:

1) Frequency-reconfigurable antenna (FRA); This antenna uses voltages applied to Barium Strontium Titanate (BST) capacitors as a tuning mechanism [9]. These capacitors absorb most of the energy for frequencies just above the input match, leading to a rejection band close to the receiving band. Therefore, this antenna is both lossy and narrowband and an example of a typical antenna that will be used in IoT devices. In this case, we configured the antenna to be matched at 1.4 GHz.
2) Discone antenna cascaded with a filter (DAF); To mimic a narrowband antenna that is designed to have both a passband and a rejection band, and to separate mismatch effects from thermal loss effects. Such an antenna with both a passband and a rejection band is another typical example of an IoT device.
3) Discone antenna cascaded with a 50 dB attenuator (DAA); To mimic an antenna designed to have a large rejection band, and to separate thermal loss effects from mismatch effects. We use a discone antenna because we expect it has similar far-field behavior as the frequency-reconfigurable antenna we use.

We calculate efficiency for these three use-cases using the two- and three- antenna method, where the second and third antenna are both dual-ridge horn antennas of the same type (DRHA1 and DRHA2). We measure all S-parameters between three antenna ports for every use-case, where port 1 is connected to the use-case antenna and port 2 and 3 connected to DRHA1 and DRHA2, respectively. We then estimate the efficiency of the use-case antenna with the two- and three-antenna methods. Having a third antenna present in the chamber increases the losses, but this should not affect the measured antenna efficiency if the chamber-decay time is calculated for the same setup that is used to measure efficiency [34]. For all measurements shown, we used a chamber-decay time which was determined from the transmission between two low-loss antennas.

To compare all use-cases, we focus on the total efficiency of one of the two dual-ridge horn antennas (DRHA1). As a reference for the total efficiency of DRHA1, we use an estimate obtained from a measurement performed with two low-loss antennas as a second and third antenna by using the three-antenna method, since this method can be directly related back to fundamental theory and has been shown to work for low-loss and broadband antennas [20] [21]. 95 % confidence interval error bars were added to the best estimate of all measurements, which were obtained from a combination of calibration uncertainty and the uncertainty of 12 independent realizations due to a lack of spatial uniformity [25] [31]. We use the technique desribed in Section III. For each case of determining total efficiency, we only state that there is an issue when the error bars of the estimate do not overlap with the error bars of the reference.

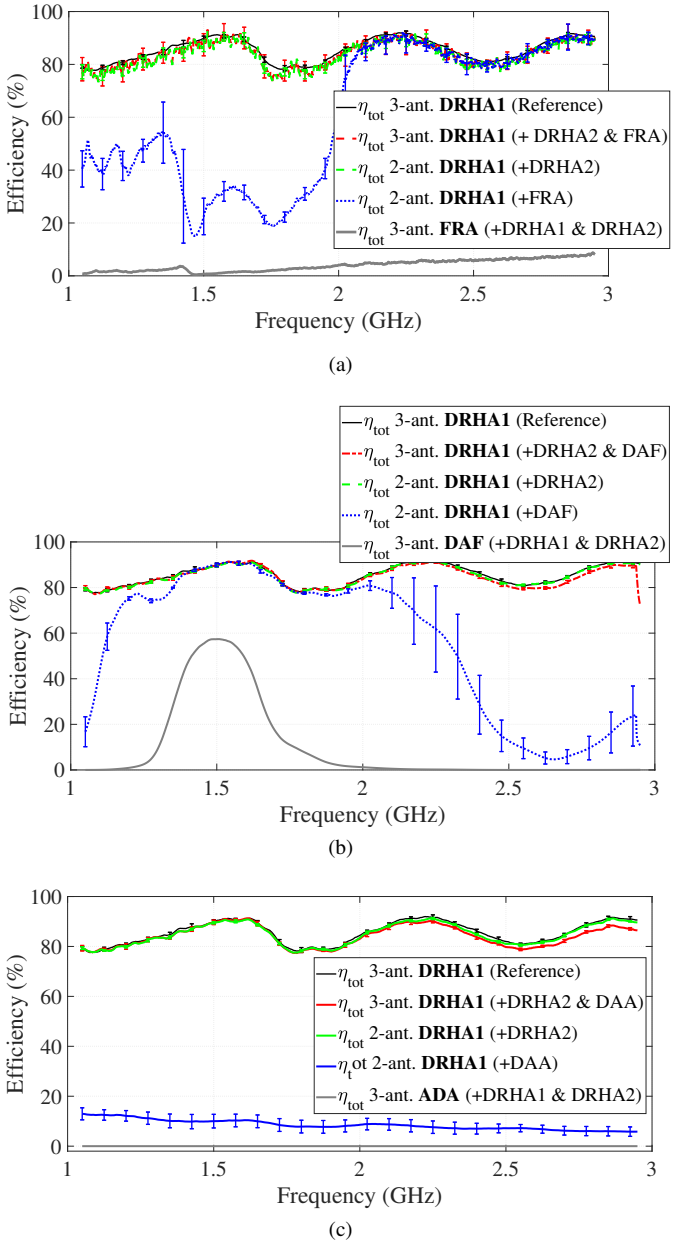

Fig. 5. Total efficiency of DRHA1 for three different use-case 1, 2 and 3, shown in (a), (b), and (c), respectively. The total efficiency of each use-case antenna was added for reference. For all cases, the two-antenna method efficiency estimate of the horn showed significant underestimations and uncertainties compared to the three-antenna method estimate, when one of the use-case antennas was used in the measurement.

Fig. 5(a) shows the effects of the presence of the FRA on the total efficiency of DRHA1, for different methods. We added the expected efficiency of the FRA as well for reference, which was studied extensively in [9]. Of all cases, only the two-antenna method showed discrepancies when we used the FRA as an AUT. Below 2 GHz, the efficiency of the FRA is very low and the efficiency estimate of DRHA1 is far off from the reference, and uncertainties are much higher than usual. The increase in uncertainty and the underestimation of efficiency are caused by high uncertainties and an overestimation of $\langle |S_{11,s}|^2 \rangle$ of the FRA due to noise, which will be explained in detail in the next (sub)sections. When the efficiency values

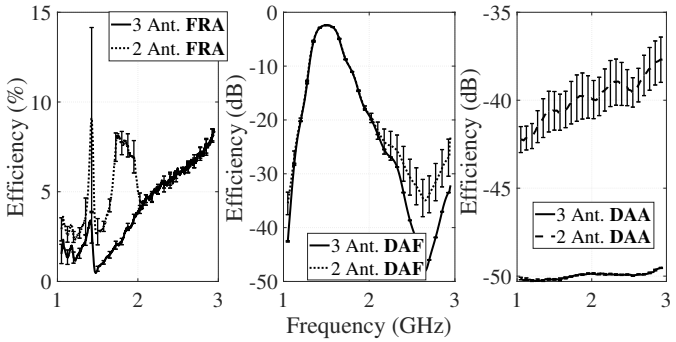

Fig. 6. Total efficiency of all use-case antennas, calculated with both the two- and three-antenna method. The two-antenna method estimate is overestimated and shows larger uncertainties compared to the three-antenna method one. Note the difference in scale units.

of the FRA are higher, which is shown above 2 GHz, the efficiency estimate is similar to the reference. Using the 3-antenna method with the FRA present does not show the issue.

Fig. 5(b) shows the effects of the presence of the DAF on the total efficiency of DRHA1. Similar to the first use-case, the only case that caused an issue was the case where the two-antenna method was used with parameters related to the DAF. The issue showed mainly in the rejection band of the DAF, due to the overestimation of $\langle|S_{11,s}|^2\rangle$ of the DAF, similar to the first use-case. The efficiency of the DAF in the rejection band is around -50 dB.

Fig. 5(c) shows the effects of the DAA on the total efficiency of DRHA1. The efficiency of the DAA over the entire frequency band is approximately -50 dB due to the attenuator, which caused discrepancies in the efficiency estimate of DRHA1 due to the issues with the two-antenna method. However, uncertainties are lower, which will be discussed later. Nevertheless, a similar issue arises in the two-antenna method when one uses antennas with a low efficiency, regardless if this efficiency is low due to a high mismatch or a loss mechanism.

According to (3), if $\langle|S_{11,s}|^2\rangle$ is overestimated, the efficiency of the reference antenna is underestimated and the efficiency of the AUT on port 1 is overestimated. The former is shown in Fig. 5 and the latter is shown in Fig. 6. Note the difference in y-axis. Due to the low efficiencies of the DAA and DAF, those efficiencies are plotted in dB. The reference efficiency estimates were calculated with the three-antenna method since all the $\langle|S_{21,s}|^2\rangle$ values did not show overestimated values. Therefore, it is unlikely that the reference estimates were significantly affected by noise.

These experiments have shown large discrepancies in the antenna-efficiency estimates of all IoT use-case antennas when the two-antenna method was used, showing an overestimation in the estimate of the AUT and an underestimation in the estimate of the reference antenna. It should be noted that the uncertainties shown in Fig. 5 and 6 are not the actual uncertainties of the antenna efficiencies, but they are an error caused by the method. However, they can be used as an indication that the method is not working. Both discrepancies and uncertainties are due to an overestimation of $\langle|S_{11,s}|^2\rangle$ due to noise, which we will show next.

B. S-parameter scatter plot

According to (5), it is possible that for low signal values, resulting in a low value of $S_{ij,\text{paddles}}$, the value of $S_{ij,\text{noise}}$ will not be negligible and $S_{ij,s}$ will be overestimated. Even worse, when the signal drops below the noise floor of the measurement setup, the contribution of $S_{ij,\text{paddles}}$ starts to become negligible. We will illustrate this with an experiment similar to use-case 3, where we carry out three measurements with different attenuation values. On port 1, we first connected the discone antenna with no attenuation, then 20 dB attenuation and last 50 dB attenuation. DRHA1 and DRHA2 were connected to port 2 and 3 for all measurements and the same VNA settings as described earlier were used. All points in the scatter plot shown represent a separate sweep for 2 GHz. We just show one frequency since the results for other frequencies are similar.

Fig. 7 shows that for higher attenuation values, the variances ($S_{21,s}$ and $S_{11,s}$) become smaller. The $S_{11,s}$ scatter plot reduces more since the $S_{11,s}$ signal experiences twice the attenuation compared to $S_{21,s}$. Therefore, the contribution of the paddles compared to the noise is less in $S_{11,s}$ and is consequently more prone to being affected by noise than $S_{21,s}$. The one- and two-antenna method both use $S_{11,s}$ and $S_{21,s}$, but the three-antenna method only uses $S_{21,s}$. Therefore, the three-antenna method is less susceptible to noise effects than the two-antenna method. However, when losses or mismatches become much larger than those of the use cases, $S_{21,s}$ can be overestimated and the three-antenna method can be affected as well.

The effect of noise on these methods is clearly shown in Fig. 8. We introduce a new experiment where we compare two cases. In the first case, we measured $S_{21,s}$ and $S_{11,s}$ with antenna 1 being the discone antenna cascaded with a 50 dB attenuator and antenna 2 DRHA1. In the second case, we measured these values between the discone antenna with no attenuation and DRHA1, and we computed what the size of the scatter plot would be with 50 dB attenuation. The variances of the measured and calculated values in the $S_{21,s}$ scatter plot are very similar. However, for $S_{11,s}$ the measured variance is overestimated by approximately 45 dB compared to the calculated one, which, according to (3) leads to an overestimation of approximately 10 dB in efficiency. This matches the results of Fig. 6(c) for 2 GHz. According to (3), an overestimation in $S_{11,s}$ leads to an overestimation in efficiency of the AUT, and in an underestimation of the reference antenna, which matches the results shown in Fig. 5 and 6. In Section V, we present a model that supports this theory by estimating the expected average radius of the scatter plot for different signal levels.

Due to the discrepancy in $\langle|S_{11,s}|^2\rangle$, large deviations occured over different turntable positions, or independent realizations, which caused high uncertainty values in Fig. 5 and 6. For example, for the measurement of the FRA, we observed differences of 30 dB in $\langle|S_{11,s}|^2\rangle$ between different independent realizations. Therefore, with the method proposed in Section III, these uncertainties are included in the uncertainties due to a lack of spatial uniformity, even though they are

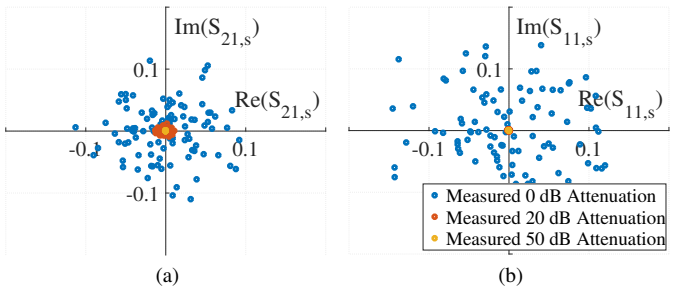

Fig. 7. Scatter plot for S_{21_s} (a) and S_{11_s} (b) for different attenuation levels at port 1 at 2 GHz. The size of the scatter plot becomes smaller for higher attenuation levels.

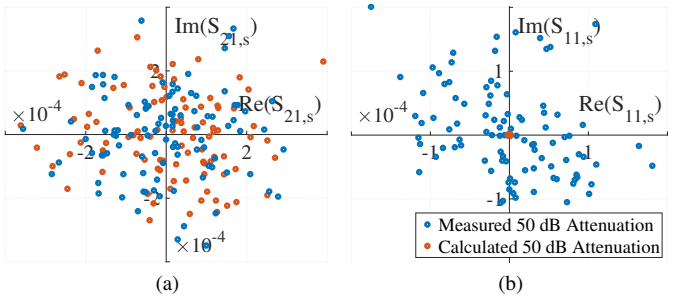

Fig. 8. Scatter plot for S_{21_s} (a) and S_{11_s} (b) for a measured and calculated case of 50 dB attenuation at 2 GHz. The measured $S_{11,s}$ is significantly overestimated due to noise, where the calculated $S_{11,s}$ is a correct reference.

caused by a different effect. All other S-parameter variances did not show this effect. This variation in position seemed to be caused by two effects. First, the noise variance is expected not to change significantly over different turntable positions. However, since the variances are so small, a small change in noise variance could become significant, hence changing $\langle |S_{11,s}|^2 \rangle$. Second, deviations in the unstirred component of S_{11}, $\langle S_{11} \rangle$, caused part of these deviations as well. $\langle S_{11} \rangle$ mainly contains contributions from the reflection coefficient of the antenna. In the case of a highly-mismatched or high-loss antenna, the unstirred energy contribution becomes very large compared the stirred energy contribution, so small deviations in $\langle S_{11} \rangle$ can lead to high uncertainties in $S_{11,s}$ as well.

V. Noise Modeling

To show that noise can cause the size of the S-parameter scatter plot to be overestimated, a model was developed in connection to this work for generic S-parameter measurements with consideration of VNA noise effects, estimating the expected average radius of the scatter plot for various SNRs [35]. For model simplicity, we focused on the average radius of the cloud instead of the variance as it is used in (1) and (3). We cannot calculate the variance from the radius, because $\langle |S_{ij,s}|^2 \rangle \neq \langle |S_{ij,s}| \rangle^2$. However, the average radius gives us a sufficient estimate of the increased size of the S-parameter scatter plot. In the first version of the model, we only take noise caused by the VNA stimulus signals and the received signals into account. We modeled the additive noise effects as complex random variables with a normal

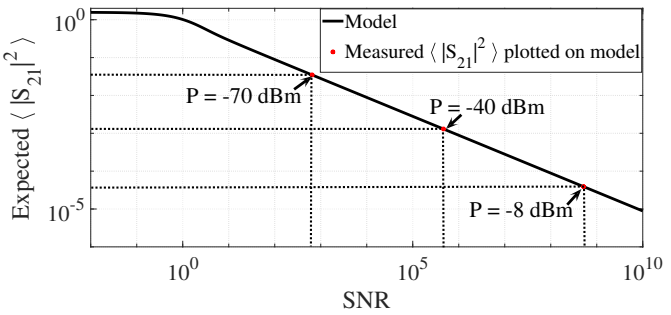

Fig. 9. Modeled SNR versus the expected average radius of $S_{21,s}$, with measured attenuator results plotted on the model. The expected average radius increases for lower SNRs.

distribution. Therefore, $S_{ij,\text{noise}}$ can be split into its real and imaginary parts as

$$S_{ij,\text{noise}} = x + jy, \tag{6}$$

where $j = \sqrt{-1}$, and x and y are independent identically distributed Gaussian random variables. They both follow a normal distribution $\mathcal{N}(0, \text{NSR}/2)$ [35], where NSR indicates the noise-to-signal ratio that is simply the reciprocal of the SNR on the linear scale.

The average radius of the S-parameter cloud due to noise can be estimated by calculating the expected value of $|S_{ij,\text{noise}}|$, or equivalently $\sqrt{x^2 + y^2}$. In light of known distributions of x and y, $|S_{ij,\text{noise}}|$ is simply a Rayleigh random variable with its mean given by

$$\langle |S_{ij,\text{noise}}| \rangle = \sqrt{\pi \cdot \text{NSR}}/2. \tag{7}$$

A more extensive explanation will be provided in [35]. Note that the expected average radius without noise influences should approach zero, as shown in Fig. 9. This figure shows that the average radius gradually increases, instead of rapidly increasing once S_{21} reaches the noise floor. We validate this by performing measurements of a 50 dB attenuator, and by showing that similar effects occur with RC measurements in Section VI. We used experimental data to find an approximate average radius for the scatter plot, where S-parameters of a 50 dB attenuator were measured on a VNA with different VNA signal power levels. The attenuator was connected between port 1 and 2 of the VNA. All VNA settings, except for the signal power, were kept the same for all measurements. The noise floor was estimated to be approximately -100 dBm and we assumed it did not change significantly for various signal powers. This way, the system SNR could be determined at different power levels. At each power level, we measured S_{21} 100 times. Next, we calculated the average radius of the scatter plot, $\langle |S_{21} - \langle S_{21} \rangle| \rangle$, to compare it with the model prediction. We plotted the measured radii for different signal powers on the expected modeled ones, as shown in Fig. 9. From there, we can read the SNR from the model and extract the noise since we know the signal power. For all measurements, the noise level stayed around -100 dBm, showing an agreement between the model and the experiment and both showing that the size of the S-parameter scatter plot increases gradually for a lower SNR.

If we extend this model to one containing the RC, the paddle movements introduce another random variable into the model. As mentioned in Section II, the paddle contributions are not truly random, however, it can be modeled as a complex random variable. In future research, we will try to use this model to extract the paddle contributions from the stirred energy component by removing the noise effects. Although it may be tempting to subtract the noise variance directly from $\langle |S_{ij,s}|^2 \rangle$, preliminary research has shown that the noise variance was correlated with paddle movements so the noise cannot be subtracted in such a way. However, one can solve the problem in a simpler way as well. In the next section, we will show how to recognize and solve the noise issue.

VI. Recognizing and Solving the Issue

If one does not know the expected efficiency of the AUT, it can be hard to tell whether or not the two-antenna method efficiency estimate is affected by noise. We list a few ways of recognizing if the issue is present or not, and we provide a possible solution.

A simple way to recognize this problem is by first performing a two-antenna method measurements with two broadband and low-loss antennas. Then, by performing the measurement again after replacing one of the antennas with the AUT. If the efficiency estimate of the broadband, low-loss antenna that was present in both measurement is significantly different, it is likely that the estimate of the AUT is not correct due to a low SNR. It is important to test this for the entire frequency range of interest, since the losses of the chamber can change significantly. Therefore, the SNR of the S-parameters varies over frequency as well. Besides that, the noise variance may vary over frequency as well, as shown for the instrumentation noise in Fig. 10.

The problem can also be recognized by inspecting the scatter plots of the stirred components. If antenna 1 has frequency bands where it is high-loss or mismatched, $S_{11,s}$ should be significantly smaller than $S_{21,s}$ for these bands, since it experiences the mismatch or attenuation twice. However, if both stirred components have a similar variance, as is the case in Fig. 8, the noise contribution is probably much larger than the paddle contribution, and the measurement is most likely affected by noise. Earlier research has shown that the noise

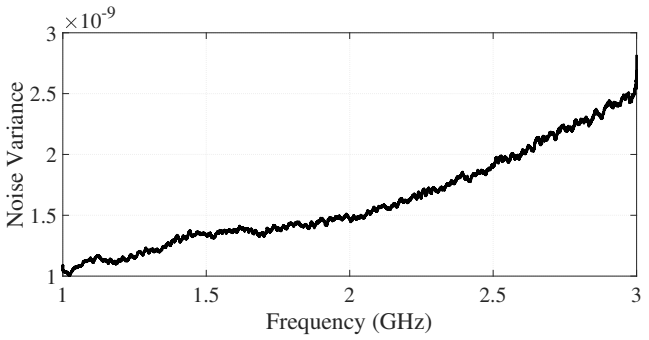

Fig. 10. Noise variance of the noise floor over frequency. The noise variance increases for higher frequencies. We expect the RC noise to vary over frequency as well.

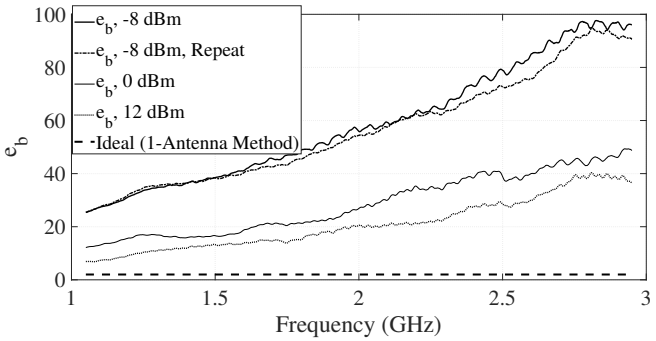

Fig. 11. Enhanced backscatter constant for 2 repeats with VNA signal power -8 dBm, and one repeat with a 12 dBm signal power, compared to the ideal value of $e_b = 2$, as it would be in the one-antenna method. e_b gets closer to 2 for higher signal power levels, hence higher SNRs.

is not just caused by the instrumentation, so if one calculates just the noise variance of the noise floor, this can lead to a false figure of merit for the minimum size of the scatter plot.

Estimating uncertainty can be a valuable tool as well for determining if one has an issue, as shown in Fig. 5, where uncertainties are expected to be mainly caused due a varying noise variance per independent realizations and due to uncertainties in $\langle S_{11} \rangle$. However, this approach can be more time intensive compared to previous approaches, since a measurement has to be performed over ideally $P = 9$ positions for one to know if issues occur. We mostly focused on total efficiency in this work, however, uncertainties on radiation efficiency are expected to be even higher due to differences in $\langle S_{11} \rangle$ over various positions [9]. Radiation efficiency is determined by correcting for antenna mismatch, using $\eta_{\text{rad}} = \eta_{\text{tot}}/(1 - |\langle S_{11,s} \rangle|^2)$. Especially for high-loss antennas, $\langle S_{11} \rangle$ can become very small, so any discrepancy could lead to large deviations in radiation efficiency as well.

Another intuitive way of characterizing if the measurement is affected by noise, is by looking at the estimated e_b. When we calculate e_b using (2), it is generally around 2, however, it can deviate significantly further from that due to two effects:

1) For higher frequencies, there have been cases where e_b was measured to be significantly larger than approximately 2 [28] [36]. A cause on why this can occur is yet to be shown.
2) The $\langle |S_{11,s}|^2 \rangle$ term in (2) is overestimated due to a low SNR, and, therefore, e_b is overestimated as well.

Since we focus on lower frequencies (1 GHz - 3 GHz) and the effect of 1) is much less significant in this case, we assume that 1) does not apply and that if e_b is not approximately 2, $\langle |S_{11,s}|^2 \rangle$ is affected by noise. Comparing these two effects for high frequencies is a topic for future research. According to the model, the size of the scatter plot should gradually decrease for higher SNRs. Therefore, we should always be able to reduce the noise issue in the two-antenna method by increasing signal power or by reducing the IF BW. Since the latter introduces a significant time penalty, we focus on the former. Fig. 2 shows e_b for use-case 3, measured with different signal powers. All cases are affected by noise, and, therefore, e_b is significantly different than approximately 2. First, when

we repeated the same measurement twice, the overestimation of $S_{11,s}$ was similar, resulting in a similar overestimation of e_b, as shown in Fig. 11. Next, when we increased the signal power, the issue reduced. Therefore, when one has a similar issue, we propose to increase signal power until e_b is approximately 2. We advise readers with similar issues to reduce chamber losses as much as possible by removing all equipment and attributes that are not necessary for the measurement to optimize the SNR as much as possible. We are currently researching model and measurement methods to make a noise correction for cases where increasing signal power is not a possibility.

It should be noted that these noise effects vary significantly for different chambers, but they also vary for different antennas. As shown in Fig. 5(a) and (b), the issue started at approximately -13 dB antenna efficiency for the FRA, and at approximately -20 dB for the DAF. Therefore, no accurate figure of merit can be determined which is valid for all setups in the chamber. This is expected to be because the antenna itself introduces noise contributions as well. The noise issue does not just affect the antenna efficiency estimate. Other metrics, such as the chamber transfer function and TIS are dependent on the estimated variance of S-parameters as well. Next, we will focus on these metrics and their uncertainties in IoT applications.

PART II: TIS CHALLENGES FOR NB-IOT

TIS measurements have been perfomed and researched extensively for earlier-generation and wideband protocols, such as WCDMA or GSM. However, for NB-IoT we expect additional challenges due to the narrowband nature of this protocol. We will explain the theory for TIS and the expected challenges of this protocol. After, we will show a novel proposed method for determining uncertainties for the chamber transfer function and TIS and we will show preliminary results for uncertainties of the chamber transfer function.

VII. TIS THEORY

TIS is a measure of the minimum power that a device can measure for a certain protocol. The minimum power measured by a base-station emulator (BSE) is defined as the power where the bit-error-rate (BER) drops below a certain value. For the NB-IoT protocol we use 95 %. We measure TIS for a starting input power and as long as the BER is above 95 % [7], we step the power down until it drops below this value. We measure TIS for multiple mode-stirring samples, and average over all of these samples after. Much research on the effects on uncertainty by using NB-IoT still needs to be performed, however, in this section, we show the theory and measurement challenges for measuring TIS.

In the CTIA standard [37], TIS is given by

$$P_{\text{TIS}} = G_{\text{ref}}\eta_{\text{meas}}^{\text{tot}}G_{\text{cable}}(\langle\frac{1}{P_{\text{BSE}}}\rangle_M)^{-1}, \tag{8}$$

where P_{TIS} is the total isotropic sensitivity in W and η_{meas} the total efficiency of the measurement antenna. Since, the antenna is part of the device for the vast majority of such devices, the efficiency of the device antenna is not included in this equation. Therefore, its characteristics are part of P_{TIS}. G_{cable} is the cable loss, which we need to compensate for since we do not perform a calibration in this measurement, $P_{\text{BSE}(n)}$ is the minimum power measured by the BSE at the threshold BER in W, M is the number of mode-stirring samples and G_{ref} is the chamber transfer function, which is a measure of the losses in the chamber. In the CTIA standard [37], G_{ref} is given by

$$G_{\text{ref}} = \frac{\langle\langle|S_{21}|^2\rangle_M\rangle_F}{\eta_{\text{meas}}^{\text{tot}}\eta_{\text{ref}}^{\text{tot}}}, \tag{9}$$

where $\eta_{\text{ref}}^{\text{tot}}$ is the total efficiency of the reference antenna and $\langle\cdot\rangle_F$ is an averaging over F frequencies across the channel bandwidth. Unlike TIS, we compensate in the chamber transfer function for the reference antenna efficiency, since the chamber losses should not be a measure of the antenna efficiency. We only compensate for efficiency in this equation, since the calibration reference plane for such measurements is brought up to the connectors of the antennas which compensates for cable losses.

The noise effects shown in Part I can cause deviations in G_{ref} results in two ways. First, when the chamber losses are determined with a high-loss or highly-mismatched antenna, the efficiency estimate can contain high uncertainties and significant over or underestimations. In (9), any deviation in efficiency directly translates to a deviation in G_{ref}. Second, when S_{21} becomes too small, the contribution of the noise is no longer negligible, and $\langle|S_{21}|^2\rangle$ becomes overestimated. Note that we do not compensate for unstirred energy here, since we underestimate the chamber losses if this is not taken into account. Due to the issues with previously shown types of IoT antennas, we recommend that chamber loss is characterized with two low-loss antennas. However, all peripheral equipment and the NB-IoT device should be present in the chamber so the chamber experiences the same loss for both the G_{ref} and the P_{TIS} measurement. If the chamber losses are over or underestimated, P_{TIS} can be over or underestimated as well.

Another factor that can cause issues with NB-IoT is the increased uncertainty. In Section IX, we will show these effects on G_{ref}. Next, we will show a proposed method for determining uncertainty for P_{TIS} and G_{ref}.

VIII. TIS UNCERTAINTY

In this section, we first present uncertainty that was acquired from different independent realizations, which was calculated using a proposed method in the CTIA. Second, we propose an extended method to take uncertainties from efficiency, calibration and cable loss into account, based on the method discussed in Section III. This method is yet to be validated.

A. Sigma G_{ref}

We performed a significance test on the G_{ref} results [31]. 'Between' differences were not significant so we calculate the

uncertainty using the standard deviation of multiple independent realizations of G_{ref} given by

$$\sigma_{G_{\text{ref}}} = \sqrt{\frac{1}{N-1}\sum_{n=1}^{N}(G_{\text{ref},n} - G_{\text{ref}})^2}, \tag{10}$$

where N is the number of independent realizations, $G_{\text{ref},n}$ the chamber transfer function for independent realization n, and G_{ref} the best estimate for the chamber transfer function which is obtained from the mean of all independent realizations. A penalty is introduced by dividing by $N-1$ instead of N, since one cannot be sure about the true value of G_{ref}. Therefore, we only speak of a best estimate, and we need to add a penalty to take this extra uncertainty into account.

B. Extended Uncertainty TIS

We can extend the uncertainty analysis for G_{ref}, and obtain the uncertainty for TIS, by using similar methods as shown in Section III. This way of characterizing uncertainty for TIS is a completely novel method. However, it needs to be verified in future research. We start by extending the uncertainty of G_{ref} by calculating uncertainty for all its terms. This is done with the following steps.

1) We obtain the uncertainties for $\eta^{\text{tot}}_{\text{meas}}$ and $\eta^{\text{tot}}_{\text{ref}}$ from the method shown in Section III. These uncertainties were not caused by only systematic effects originally. However, they occur as a systematic effect in this method since we obtain the antenna efficiencies with uncertainty only once and we use the same efficiency results for all measurements. Since we have measured a significant amount of independent realizations, and we assume that the calibration uncertainty is systematic, we do not expect significant differences by using this approach.
2) We calculate the calibration uncertainty for S_{21} using the MUF by performing step 1 and 2 of part A the method shown in Section III.
3) We use the post processor in the MUF to propagate the uncertainties of the separate terms to a value of G_{ref}. This is similar to step 3 in part A of Section III, but we calculate G_{ref} instead of efficiency.
4) We combine all independent realizations for G_{ref}, and apply the uncertainties due to a systematic effect from one independent realization for G_{ref} to all other independent realizations to obtain a best estimate including uncertainties, as shown in Fig. 3. Note that the combined result also includes a coverage factor, which is not included in $\sigma_{G_{\text{ref}}}$. Therefore, we do not include the penalty which is introduced in (10).

Next, we can use the best estimate with uncertainties for G_{ref} to calculate uncertainty for TIS.

1) Since we perform only one G_{ref} measurement, and we use it for all TIS measurements after, we treat the G_{ref} uncertainty as an uncertainty due to a systematic effect as well. This is similar to the approach of treating the uncertainties of efficiency as a systematic effect.
2) We obtain the uncertainty for cable loss (G_{cable}) by measuring the cable loss multiple times, and characterizing the deviations in loss between the measurements. We apply a coverage factor. Between every measurement, we move the cable as it would move in reality after calibration. For example, due to a movement from the electronic calibration module to the antenna, or due to the turntable changing positions. Since we characterize these uncertainties only once, we treat them as uncertainties due to a systematic effect as well.
3) If we combine (8) and (9), the term $\eta^{\text{tot}}_{\text{meas}}$ drops out. However, since we are often interested in both G_{ref} and TIS uncertainties, we calculate TIS from the result of G_{ref}, so we have to include the uncertainties of $\eta^{\text{tot}}_{\text{meas}}$ again as a systematic effect.
4) We do not include uncertainties from the BSE in this approach, however, we do take uncertainties in P_{TIS} from different independent realizations into account, which is expected to contain some uncertainties of the BSE.
5) We calculate the expanded uncertainties by calculating the uncertainties due to a systematic effect of one independent realization, and apply it to the combined best estimate of all independent realizations, in a similar way as shown in Fig. 3.

This method calculates the uncertainties from the calibration and from a lack of spatial uniformity of every element in the calculation and then propagates them through to an expanded uncertainty for P_{TIS}. As mentioned before, this is a novel method which will be validated in future research.

IX. G_{REF} Uncertainty Results

The channel bandwidth of NB-IoT is 180 kHz. According to the standard, G_{ref} needs to be frequency averaged over the same bandwidth as TIS. However, since the channel bandwidth for NB-IoT is much narrower than previously used protocols, we perform less frequency averaging so we expect the uncertainty to increase. In this section, we show preliminary results and a possible explanations of this phenomenon.

A. Chamber Loading

Usually, we need to load the chamber by adding RF absorber to keep the communication link while measuring TIS. This is due to the fact that, in an unloaded chamber, the frequency selectivity is usually too high. To prevent this from happening, we flatten the frequency response by loading

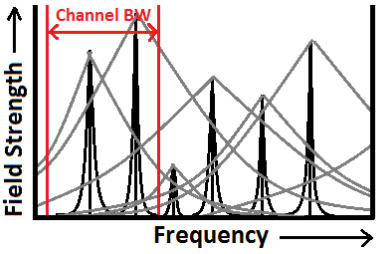

Fig. 12. Illustration of the mode-distribution in a reverberation chamber for an unloaded (black distribution) and a loaded one (grey distributions). More modes, hence more independent samples, occur in the channel bandwidth for higher loading cases.

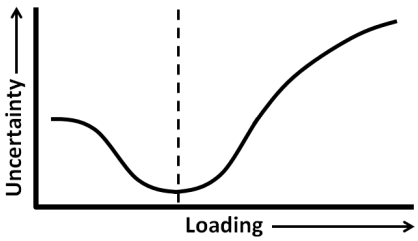

Fig. 13. Illustration of the expected effect on uncertainty by an increase in chamber loading. Uncertainty first decreases because there are more independent samples within the channel bandwidth, but increases after due to high correlations.

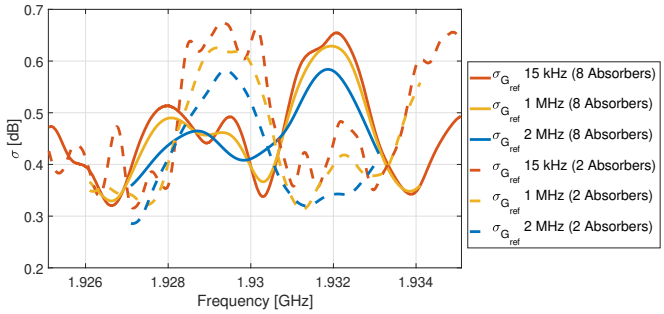

Fig. 14. $\sigma_{G_{\text{ref}}}$ for two loading cases (2 and 8 absorbers) for various averaging bandwidths (15 kHz - 2 MHz), determined with 12 independent realizations each. The uncertainty reduces for higher averaging bandwidths, however, the maximum uncertainty in the band is similar for both loading cases, which is usually not the case for wideband measurements.

the chamber. This increases correlation and reduces spatial uniformity, which increases uncertainty.

A measure of the frequency correlation is the coherence bandwidth. In general, the coherence bandwidth needs to be higher than the channel bandwidth. The coherence bandwidth of an average unloaded chamber is higher than 180 kHz [24], so it should be possible to perform the measurement with no loading, which, due to a higher spatial uniformity, reduces uncertainty. However, earlier work did use chamber loading. [6]. Therefore the question arises if chamber loading is preferable, and we need to focus on mode distribution.

B. Mode Distribution

In an unloaded chamber, each mode is expected to be very narrowband. When we load the chamber, these bands become wider, and, therefore, the frequency response flattens. This is illustrated in Fig. 12. We focus on three mode distribution effects which could affect uncertainty.

- For narrow channel bandwidths, less modes are included in the frequency averaging compared to wider bandwidths. Therefore, we have less independent samples, hence a higher uncertainty. This could be solved by using more mode-stirring samples. However, this solution is limited, since the maximum amount of mode-stirring samples is limited as well to prevent high correlations.
- If a narrow channel bandwidth is used, it could be possible that one uses modes with a high field strength for one channel, while modes with a low field strength are used for another. Therefore, the value of G_{ref} could change significantly over different channels, and, therefore, the entire band used.
- If the chamber is loaded, the frequency response flattens, as illustrated in Fig. 12. Therefore, correlation increases and uncertainty increases. However, for such narrow channel bandwidths, loading could be preferable for decreasing uncertainty. As illustrated in Fig. 12, more modes are included in a single channel when the chamber is loaded. This leads to more independent samples, which reduces uncertainty.

For this narrowband case, both frequency correlation and a lack of independent samples contribute to uncertainty, where the former is an effect of a higher loading cases, and the latter an effect of unloaded or lower loading cases. Therefore, when we increase loading, we expect that uncertainty first decreases because there are more independent samples within the channel bandwidth, but increases after due to high correlations. This is illustrated in Fig. 13, where we expect to have a lowest uncertainty 'sweet spot' for a certain amount of loading. This approach could be more elaborate than the current approach where one defines the amount of loading just by use of the coherence bandwidth, however, this has yet to be validated.

C. Experimental results

Fig. 14 shows $\sigma_{G_{\text{ref}}}$ for loading cases with two and eight absorbers, averaged over various channel bandwidths. In the current CTIA testplan proposal [3], it is proposed to choose the highest value of $\sigma_{G_{\text{ref}}}$ as uncertainty, since, as shown in the results, uncertainty estimates can change significantly over frequency. The results show reduced uncertainty when a higher averaging bandwidth is used, which is expected since this increases the amount of independent samples. A running average was used for calculation. We used similar VNA settings as before, but with a 1 kHz frequency spacing over a 10 MHz band.

Usually, $\sigma_{G_{\text{ref}}}$ increases for higher loading cases [37], but these results show similar maximum values for both loading cases. We expect that this is due to the effect shown in Fig. 13, where the two-absorber case may have uncertainty contributions from mostly a lack of independent samples, while the eight-absorber case may have mostly uncertainty contributions from high frequency correlation.

These assumptions are based on theoretical principles, but more research should be performed to find the exact causes of these uncertainties. We only showed results for the lower end of band 2 of the NB-IoT protocol here for two absorber cases. To form true conclusions, these measurement should be performed for more absorber cases in multiple bands, and a full TIS measurement should be performed as well. There are many other IoT-relates research topics for TIS, such as measuring Average Fading Sensitivity (AFS) versus TIS since these measurements are less time-intensive, measuring effects of a phantom on TIS measurements since IoT devices can be body wearables as well, and validating proposed uncertainty method will be validated. These research topics will be discussed in future publications.

X. Conclusion and discussion

In this paper, we have shown that new challenges occur in TIS and antenna-efficiency measurements for IoT applications. In Part I we have shown that issues can arise in determining antenna efficiency with the one-, two-, and three-antenna methods when the SNR of the S-parameters is too low. In such cases, the contribution of the noise to the variance can become higher than the contribution from the paddles, leading to an overestimation of the stirred energy component variance, hence an over or underestimation of the antenna efficiency estimate. We have shown the importance of taking noise effects into account in antenna-efficiency reverberation-chamber measurements. In Part II, we have shown that noise effects can possibly affect TIS measurement as well, and we showed a preliminary study on uncertainty for narrowband measurements. We presented novel methods of determining uncertainty for both of these metrics.

This work has shown that methods that performed adequately for wideband applications can cause issues and new challenges when these are used for IoT applications. These factors should be taken into account when one has a similar goal of determining antenna efficiency and TIS for such applications, if one aims to reduce inaccuracies and uncertainties.

References

[1] Ericsson Mobility Report, *On the Pulse of the Networked Society*, November 2016.

[2] J. G. Andrews et al., "What Will 5G Be?," in *IEEE Journal on Selected Areas in Communications*, vol. 32, no. 6, pp. 1065-1082, June 2014.

[3] Proposed update for section 6.22, *CTIA OTA Test Plan V3.9, 2019*

[4] Release 13, 14 and 15, in *3GPP TS 36.101*

[5] Release 15, Clause 6.2F, *3GPP TS 36.521-1*

[6] J. Luo, E. Mendivil and M. Christopher, "Over-the-Air Performance Evaluation of NB-IoT in Reverberation Chamber and Anechoic Chamber," 2018 AMTA Proceedings, Williamsburg, VA, 2018, pp. 1-3.

[7] Release 15, Clause 7.3F, *3GPP TS 36.521-1*

[8] R. D. Horansky, T. B. Meurs, M. V. North, C. Wang, M. G. Becker and K. A. Remley, "Statistical Considerations for Total Isotropic Sensitivity of Wireless Devices Measured in Reverberation Chambers," 2018 International Symposium on Electromagnetic Compatibility (EMC EUROPE), Amsterdam, 2018, pp. 398-403.

[9] L. A. Bronckers, A. Roc'h and A. B. Smolders, "A New Design Method for Frequency-Reconfigurable Antennas Using Multiple Tuning Components," in *IEEE Transactions on Antennas and Propagation.*

[10] C. S. Lee, A. Duffy and C. Lee, "Antenna Efficiency Measurements in a Reverberation Chamber Without the Need for a Reference Antenna," in *IEEE Antennas and Wireless Propagation Letters*, vol. 7, pp. 448-450, 2008.

[11] A. Khaleghi, "Time-Domain Measurement of Antenna Efficiency in Reverberation Chamber," in *IEEE Transactions on Antennas and Propagation*, vol. 57, no. 3, pp. 817-821, March 2009.

[12] H. G. Krauthäuser and M. Herbrig, "Yet another antenna efficiency measurement method in reverberation chambers," *2010 IEEE International Symposium on Electromagnetic Compatibility*, Fort Lauderdale, FL, 2010, pp. 536-540.

[13] M. Piette, "Antenna radiation efficiency measurements in a reverberation chamber," *2004 Asia-Pacific Radio Science Conference*, 2004. Proceedings., Qingdao, China, 2004, pp. 19-22.

[14] C. L. Holloway, H. A. Shah, R. J. Pirkl, W. F. Young, D. A. Hill and J. Ladbury, "Reverberation Chamber Techniques for Determining the Radiation and Total Efficiency of Antennas," in *IEEE Transactions on Antennas and Propagation*, vol. 60, no. 4, pp. 1758-1770, April 2012.

[15] IEC 61000-4-21: EMC Part 4: Testing and Measurement Techniques; Section 21: Reverberation Chamber Test Methods, 2001.

[16] Q. Xu, Y. Huang, X. Zhu, L. Xing, Z. Tian and C. Song, "A Modified Two-Antenna Method to Measure the Radiation Efficiency of Antennas in a Reverberation Chamber," in *IEEE Antennas and Wireless Propagation Letters*, vol. 15, pp. 336-339, 2016.

[17] C. A. Balanis, "Antenna Theory Analysis and Design", 2nd edition.

[18] C. L. Holloway, H. A. Shah, R. J. Pirkl, K. A. Remley, D. A. Hill and J. Ladbury, "Early Time Behavior in Reverberation Chambers and Its Effect on the Relationships Between Coherence Bandwidth, Chamber Decay Time, RMS Delay Spread, and the Chamber Buildup Time," *IEEE Transactions on Electromagnetic Compatibility*, vol. 54, no. 4, pp. 714-725, Aug. 2012.

[19] L. A. Bronckers, A. Roc'h and A. B. Smolders, "Chasing the Wave in a Reverberation Chamber," *2018 International Symposium on Electromagnetic Compatibility (EMC EUROPE)*, Amsterdam, 2018, pp. 708-712.

[20] C. L. Holloway et al., "Validation of a two-antenna reverberation-chamber technique for estimating the total and radiation efficiency of antennas," *International Symposium on Electromagnetic Compatibility - EMC EUROPE*, Rome, 2012, pp. 1-6.

[21] C. L. Holloway, H. A. Shah, R. Pirkl, W. F. Young, D. A. Hill and J. Ladbury, "A three-antenna technique for determining the total and radiation efficiencies of antennas in reverberation chambers," in *IEEE Antennas and Propagation Magazine*, vol. 54, no. 1, pp. 235-241, Feb. 2012.

[22] D. A. Hill, "Plane wave integral representation for fields in reverberation chambers," in *IEEE Transactions on Electromagnetic Compatibility*, vol. 40, no. 3, pp. 209-217, Aug. 1998.

[23] D. A. Hill, Electromagnetic Fields in Cavities: Deterministic and Statistical Theories. *IEEE Press*, New York, 2009.

[24] K. A. Remley, J. N. H. Dortmans, C. Weldon, R. D. Horansky, T. B. Meurs, C. Wang, D. F. Williams, C. L. Holloway and P. F. Wilson, "Configuring and Verifying Reverberation Chambers for Testing Cellular Wireless Devices," *IEEE Transactions on Electromagnetic Compatibility*, vol. 58, no. 3, pp. 661-672, June 2016.

[25] L. A. Bronckers, K. A. Remley, B. Jamroz, A. Roc'h and A. B. Smolders "Uncertainty in Reverberation-Chamber Antenna-Efficiency Measurements in the Presence of a Phantom," *In process, 2019*

[26] J. C. West, J. N. Dixon, N. Nourshamsi, D. K. Das and C. F. Bunting, "Best Practices in Measuring the Quality Factor of a Reverberation Chamber," *IEEE Transactions on Electromagnetic Compatibility*, vol. 60, no. 3, pp. 564-571, June 2018.

[27] J. Ladbury and D. A. Hill, "Enhanced Backscatter in a Reverberation Chamber: Inside Every Complex Problem is a Simple Solution Struggling to Get Out," *2007 IEEE International Symposium on Electromagnetic Compatibility*, Honolulu, HI, 2007, pp. 1-5.

[28] L. A. Bronckers, A. Roc'h and A. B. Smolders, "Reverberation Chamber Enhanced Backscattering: High-Frequency Effects," *2019 International Symposium on Electromagnetic Compatibility (EMC EUROPE)*, Barcelona, 2019.

[29] C. L. Holloway, D. A. Hill, J. M. Ladbury, P. F. Wilson, G. Koepke and J. Coder, "On the Use of Reverberation Chambers to Simulate a Rician Radio Environment for the Testing of Wireless Devices," in *IEEE Transactions on Antennas and Propagation*, vol. 54, no. 11, pp. 3167-3177, Nov. 2006.

[30] D. F. Williams, "NIST Microwave Uncertainty Framework, version 1.4.26.24158," 2019.

[31] K. A. Remley, C. J. Wang, D. F. Williams, J. J. aan den Toorn and C. L. Holloway, "A Significance Test for Reverberation-Chamber Measurement Uncertainty in Total Radiated Power of Wireless Devices," in IEEE Transactions on Electromagnetic Compatibility, vol. 58, no. 1, pp. 207-219, Feb. 2016.

[32] IEEE Instrumentation and Measurement Society, "IEEE Standard for Precision Coaxial Connectors (DC to 110 GHz)", *IEEE Std 287*, 2007

[33] JCGM 100:2008, "Evaluation of measurement data - guide to the expression of uncertainty in measurement," 2008.

[34] A. Hubrechsen, L.A. Bronckers, K.A. Remley, R.D. Jones, R.D. Horansky, A.C.F. Reniers, A. Roc'h,and A.B. Smolders "The Effect of Peripheral Equipment Loading on Reverberation-Chamber Metrics", *2019 International Symposium on Electromagnetic Compatibility (EMC EUROPE)*, Barcelona, 2019.

[35] D. Gu and J. Jargon "Noise Influence to Scattering-Parameter Measurements," to be submitted to *IEEE Transactions on Microwave Theory and Techniques*, 2019.

[36] Zhihao Tian, Yi Huang and Qian Xu, "*Enhanced backscatter coefficient measurement at high frequencies in reverberation chamber*," 2017 International Workshop on Electromagnetics: Applications and Student Innovation Competition, London, 2017, pp. 166-167.

[37] CTIA - The Wireless Association, "Test Plan for Wireless Large-Form-Factor Device Overthe-Air Performance", *Version 1.1, July 2017*